Nano Research 2015, 8(3): 832–838
DOI 10.1007/s12274-014-0565-1
Research Article

ISSN 1998-0124
CN 11-5974/O4

Three-dimensional hierarchical Pt–Cu superstructures

Farhat Nosheen, Zhicheng Zhang, Guolei Xiang, Biao Xu, Yong Yang, Faisal Saleem, Xiaobin Xu, Jingchao Zhang, and Xun Wang (✉)

Department of Chemistry, Tsinghua University, Beijing 100084, China

Received: 5 July 2014
Revised: 15 August 2014
Accepted: 16 August 2014

KEYWORDS

noble metal,
alloy,
hierarchical structures,
electrocatalysis

ABSTRACT

Three-dimensional (3D) hierarchical Pt–Cu tetragonal, highly branched, and dendritic superstructures have been synthesized by a facile template-free hydrothermal approach, showing growth patterns along (111, 110), (111), and (100) planes, respectively. These structures have been characterized by transmission electron microscopy (TEM), X-ray diffraction (XRD), energy dispersive X-ray spectroscopy (EDX), inductively coupled plasma optical emission spectrometry (ICP-OES) and a detailed formation mechanism has been developed, which shows that the *in situ* formed I_2 and the galvanic replacement reaction between Cu and Pt^{4+} may guide the formation of these superstructures. The comparative electrocatalytic properties have been investigated for methanol and ethanol oxidation. Due to their interconnected arms, sufficient absorption sites, and exposed surfaces, these superstructures exhibit enhanced electrocatalytic performance for electro-oxidation of methanol and ethanol when compared with commercial Pt/C and Pt black.

Three-dimensional (3D) hierarchical architectures show promising applications, particularly in catalysis, and electrocatalysis due to their interconnected inner structures [1–6]. Extensive developments have been made in the past for the fabrication of dendrites and highly branched structures including biominerals [7], metal oxides [8], chalcogenides [8, 9], Au–Pd [10], Pt–Au [11], Pt–Ni [12], Ag [13], Au [14], Pd–Pt [15], Pt [14, 16, 17], and Pd [18], but few reports are available of noble metal alloy 3D superstructures [19, 20]. Recently, more efforts are being directed towards noble metal-based bimetallic nanocrystals, (noble metals with 3d-transition metals) to reduce the cost and increase the efficiency of catalysts, as bimetallic nanocrystals (NCs) show superior catalytic properties over pure metals [21–29]. Up to now, noble metal-based complex structures have been synthesized mostly by using a template or seed method that may require multi-step or complicated synthetic methods [19, 30]. Comparatively, the synthesis of highly ordered and homogeneous alloy 3D superstructures in a controllable way by one pot method still remains a great challenge. To the best of our knowledge, uniform Pt–Cu alloys with a tetragonal superstructure morphology, have not been achieved to date.

Herein, we demonstrate a simple template free

Address correspondence to wangxun@mail.tsinghua.edu.cn

aqueous route by stepwise controlled method to fabricate the uniform and hierarchical Pt–Cu 3D bimetallic superstructures (tetragonal, highly branched, and dendritic shape) (Scheme 1).

In this approach, Pt–Cu tetragonal superstructures were synthesized simply by treating an aqueous solution of polyvinylpyrrolidone (PVP, K30), sodium iodide (NaI), copper chloride and chloroplatinic acid hexahydrate at 200 ℃ for 1 h under hydrothermal conditions. Highly branched and dendritic NCs were synthesized by the addition of tryptophan to the above system while increasing the amount of NaI (for synthesis details, see the Experimental Section and Fig. S1 in the Electronic Supplementary Information (ESM)). It is found that the *in situ* formed I_2 and the galvanic replacement reaction between Cu and Pt^{4+} may guide the formation of these superstructures. Transmission electron microscopy (TEM) (Fig. 1(a)) and scanning electron microscopy (SEM) (Figs. 1(c) and 1(d)) analyses of as-prepared samples indicate that the product has uniform 3D tetragonal superstructures with an edge length of approximately 200 nm and an individual tetragonal particle consists of many interconnected arms. The number of arms on a single tetragonal superstructure can reach up to 35. 3D and unique tetragonal superstructures can be further confirmed by high-angle annular dark-field scanning TEM (HAADF-STEM) imaging (Fig. 1(b)).

The X-ray diffraction (XRD) pattern of as-prepared tetragonal superstructures (Fig. S2 in the ESM) reveals

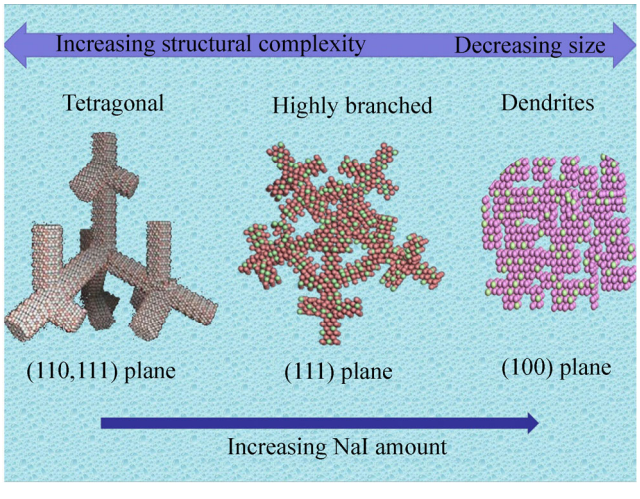

Scheme 1 Schematic illustration of the controlled growth of 3D hierarchical Pt–Cu superstructures.

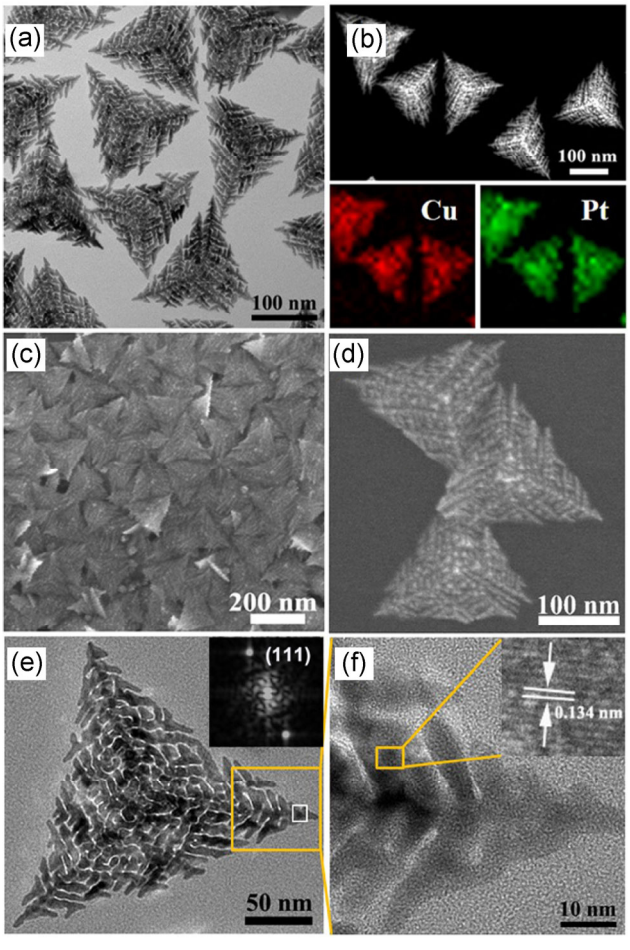

Figure 1 Images of Pt–Cu tetragonal superstructures: (a) TEM; (b) HAADF-STEM image, the red and green colors in (b) correspond to Cu and Pt elements, respectively; (c) low-, and (d) high magnification SEM images; (e) HRTEM image of a single Pt–Cu tetragonal superstructure, inset is corresponding FFT pattern of the tip marked by the white sub-square; (f) magnified HRTEM taken from the selected area marked by the square in (e), and the inset in (f) shows the lattice spacing of the portion marked by the yellow square.

the alloy formation of Pt–Cu nanostructures, as the diffraction peaks are positioned between pure face centered cubic (fcc) Pt (JCPDS: 65-2868) and Cu (JCPDS: 65-9743) crystal phases. No other single-element peak from either Cu or Pt was identified. Energy dispersive X-ray spectroscopy (EDX) attached to the TEM (Fig. S3 in the ESM) confirmed the Pt–Cu alloy formation. Furthermore, close observation of the tetragonal superstructure by high-resolution TEM (HRTEM) shows that the growth direction of the main axis and the trunk is along the (111) plane as shown by the FFT pattern (Fig. 1(e), inset) and the branches grow along the (110) plane (Fig. 1(f), inset).

TEM images also display uniform highly branched Pt–Cu structures with an average size of 150 nm (Fig. 2(a)), and dendritic NCs of approximately 20 nm size (Fig. 3(a)). HAADF-STEM micrographs and EDX element mapping (Figs. 2(b) and 3(b)) reveal that Pt and Cu are evenly dispersed in both nanostructures. HRTEM images (Fig. 2(c)), and panels in Figs. 2(c1)–2(c3) of a single highly branched particle show that lattice fringes continuously cover the whole particle with a spacing distance of 0.222 nm, consistent with the (111) crystal planes and the absence of any stacking faults, demonstrating the presence of single crystal structures. Similarly, HRTEM images of dendritic particles from different regions also show that whole particle is a single crystal, having (100) planes with lattice spacing equal to 0.195 nm (Figs. 3(c) and 3(c1)–3(c3). XRD (Figs. S4 and S5 in the ESM) and EDX patterns (Figs. S6 and S7 in the ESM) confirm the

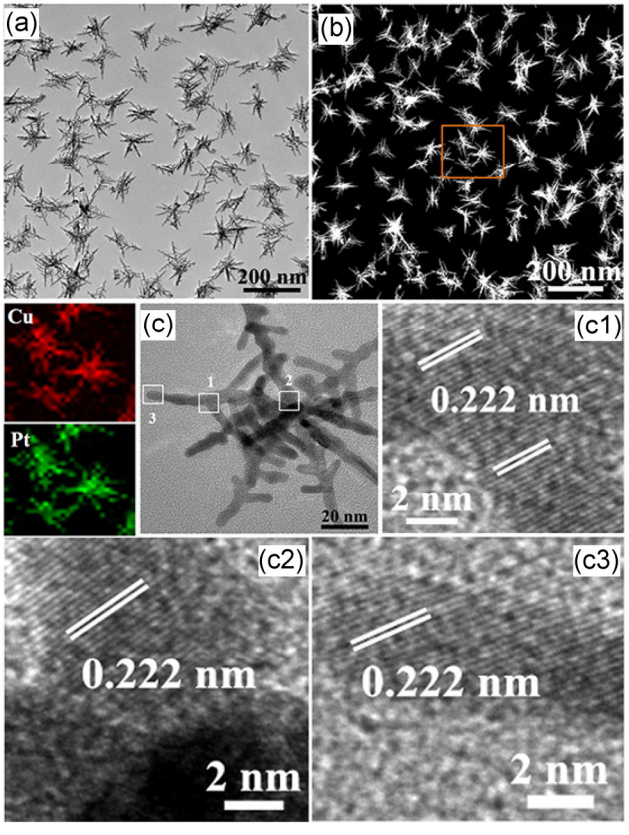

Figure 2 Images of highly branched structures: (a) TEM; (b) HAADF-STEM with corresponding elemental mapping for Cu and Pt elements; (c) HRTEM image of single particle; square panels ((c1)–(c3)) show the HRTEM images of the junction of main branch and sub-branch, center, and tip marked by the white squares in panel c.

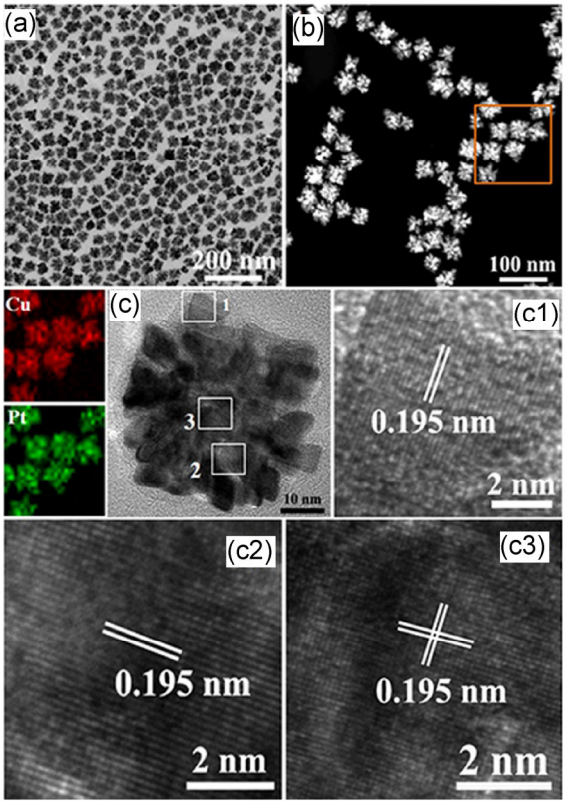

Figure 3 Images of dendritic Pt–Cu structures: (a) TEM; (b) HAADF-STEM with corresponding elemental mapping for Cu and Pt elements; (c) HRTEM micrograph of individual particle; square panels ((c1)–(c3)) show HRTEM images of dendritic particles from regions marked by white squares in panel c.

composition and show diffraction peaks, which confirm the Pt–Cu alloy formation for highly branched and dendritic structures, respectively.

To reveal the growth mechanism of the bimetallic Pt–Cu tetragonal superstructure, experiments were performed at different reaction times at 200 ℃. The TEM images of Pt–Cu NCs at various reaction times are shown in Fig. S8 (in the ESM), which highlight the shape evolution process. It can be clearly seen that when the reaction time was 0 min, small particles with a diameter of approximately 10 nm were formed (Fig. S8(a) in the ESM). The composition of these nanoparticles was studied by EDX, which confirms they consisted of copper(I) iodide (Fig. S9(a) in the ESM). When the reaction time was increased to 3 min (Fig. S8(b) in the ESM), the small particles grew into bigger particles (the EDX results in Fig. S9(b) (in the ESM) show that the large particles are also CuI). On further prolonging the reaction time to 6 min (Fig. S8(c)

in the ESM), a mixture of tetragonal superstructures and large particles was observed, which signifies that the formation of nanocrystals is still in progress (EDX results are shown in Fig. S9(c) in the ESM). The CuI was almost consumed at 14 min (Fig. S9(d) in the ESM), and after a reaction time of 16 min, diverse and highly-ordered tetragonal superstructures were formed (Fig. S8(d) in the ESM).

To further study the shape evolution and composition of superstructures, the reaction was conducted for a longer time but it was found that the shape, size and composition of the particles remained unchanged even when the reaction time was increased to 1 h (Fig. 1(a)). However, longer reaction times may increase the crystallinity of NCs, and therefore, we used 1 h for the standard procedure. The XRD patterns (Figs. S10(a)–S10(f) in the ESM) for different reaction times also correlated with the EDX data and confirm that only CuI is present in the initial stages of the reaction. On increasing the reaction time, peaks of CuI become weaker and the peaks of the Pt–Cu alloy become more intense; from reaction times from 6 to 14 min, the weak peaks of CuI can still be observed, but after 14 min, the peaks of CuI have completely disappeared and only Pt–Cu alloy peaks can be seen.

It is widely known that metals can be etched by NaI/I_2 solution. It is believed that the added NaI and I_2 formed *in situ* are responsible for the etching, as marked by red arrows in Figs. S8(b) and S8(c) in the ESM). In the early stages, CuI_2 may be produced but is unstable, and immediately decomposes to CuI, and I_2 (Fig. S11 in the ESM). The CuI may further decompose to Cu, and I_2 at high temperature. It is considered that the I_2 can also be produced by oxidation of I^-. NaI can be easily oxidized to I_2 by oxidants, especially under heating, as high temperature can drive the oxidation of I^- to I_2 [31]. To confirm this experimentally, a control experiment was carried out. A colorless NaI aqueous solution (Fig. 4(b)) was heated at 200 °C for 1 h, upon which the colorless NaI solution became yellow (Fig. 4(c)), and had the same color as a NaI/I_2 solution (Fig. 4(a)), indicating that I^- can be oxidized to I_2 by dissolved O_2. The oxidation of I^- to I_2 was further confirmed by the reaction between I_2 and starch (Figs. 4(d) and 4(e)).

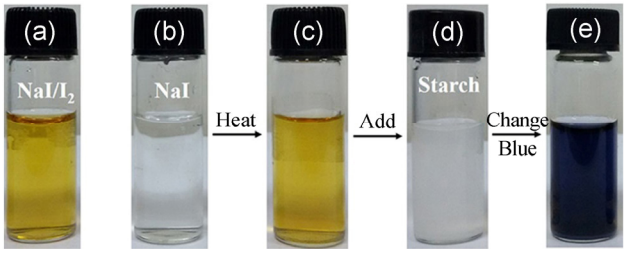

Figure 4 Confirmation of the formation of I_2 (the oxidation of I^- to I_2 is revealed by the color change).

Subsequently, as a result of the concomitant formation of reduced copper, galvanic replacement reaction between the copper and Pt^{4+} species may takes place, leading to the formation of Pt–Cu alloy NCs of complex shapes. Similar evolution processes were observed for the highly branched NCs (Figs. S12(a)–S12(d) and S13(a)–S13(e) in the ESM).

On the basis of above details, we propose that the formation of Pt–Cu superstructures involves the following steps: (1) Formation of CuI nanocrystals, and etching by the I_2 formed simultaneously *in situ* (Eqs. (1) and (2)); (2) simultaneous reduction of Cu^+ to metallic Cu, oxidation of I^- to I_2 at high temperature, and the galvanic replacement reaction between Pt^{4+} and Cu to form Pt–Cu alloy (Eqs. (3) and (4)). The reaction is very fast, and superstructures are formed within very short time, so it is difficult to observe the each step individually. All these steps can be described well by the following equations

$$Cu^{2+} + 2I^- \rightarrow CuI_2 \quad (1)$$

$$2CuI_2 \rightarrow 2CuI + I_2 \quad (2)$$

$$2CuI \rightarrow 2Cu^0 + I_2 \quad (3)$$

$$Cu^0 + Pt^{4+} \rightarrow PtCu\ alloy \quad (4)$$

To study the effect of different reagents on the shape of superstructures, some control experiments were carried out. The shape and size of the NCs can be controlled by fine-tuning of the reaction parameters. NaI has a significant effect on the formation of complex structures and we were able to obtain different structures by only changing the amount of NaI. We investigated the role of NaI by varying its amount while keeping the other conditions unchanged. In the absence of NaI, we found that product contained only small particles without any indication of dendrite formation or etching phenomena (Fig. S14(a)

in the ESM). At a very low NaI amount of 5 mg, immature etched particles were obtained (Fig. S14(b) in the ESM). When the amount of NaI was increased to 20 mg, flawless and symmetric tetragonal superstructures were observed as shown in Fig. 1. As the NaI amount was further enhanced to 50 mg, the selectivity for the small dendrites increased (Fig. S14(c) in the ESM). On further increasing the amount of NaI to 150 mg, cubes with rough surfaces were the major product (Fig. S14(d) in the ESM). Similar effects of added NaI have been observed for highly branched NCs (Figs. S15(a)–S15(d) in the ESM). This indicates that NaI controls the size, shape, and the number of branches. It also acts as shape directing and etching agent, since as we increased the amount of NaI, the shape of the NCs changed from tetragonal superstructures to highly branched and small dendrites. It is believed that rate of etching depends on the amount of NaI. Some other control experiments for tetragonal NCs were conducted by varying the metal precursors and the temperature in order to study the effect on the morphology. In the absence of Cu or Pt precursors, no tetragonal particles were obtained (Figs. S16(a) and S16(b) in the ESM). Under these conditions, temperature did not have any significant effect on particle morphology, but some unreacted CuI particles were present when temperature was decreased to 150 ℃ (Figs. S17(a) and S17(b) in the ESM). Moreover, PVP has a key role, as in the absence of PVP (Fig. S18(a) in the ESM) or with low amounts of PVP (Fig. S18(b) in the ESM) highly aggregated products were attained. Well-dispersed and regular NCs were achieved when suitable amount of PVP was incorporated in the reaction system (Fig. 1). The above results suggest that PVP plays a dual role both as a stabilizer and reductant. When CuI was used as the copper precursor instead of $CuCl_2$, similar tetragonal NCs were formed (Figs. S19(a)–S19(d) in the ESM). We also studied the effect of tryptophan on the morphology. An appropriate amount of tryptophan is also very important for the synthesis of highly branched structures (Figs. S20(a)–S20(d) in the ESM).

To investigate the electrochemical properties of as-prepared Pt–Cu nanostructures, the electro-oxidation reactions of methanol and ethanol on Pt–Cu NCs, commercial Pt black and Pt/C (Alfa Aesar) catalysts were tested. Figures 5(a) and 5(b) show the cyclic voltammogram (CV) curves for the electro-oxidation

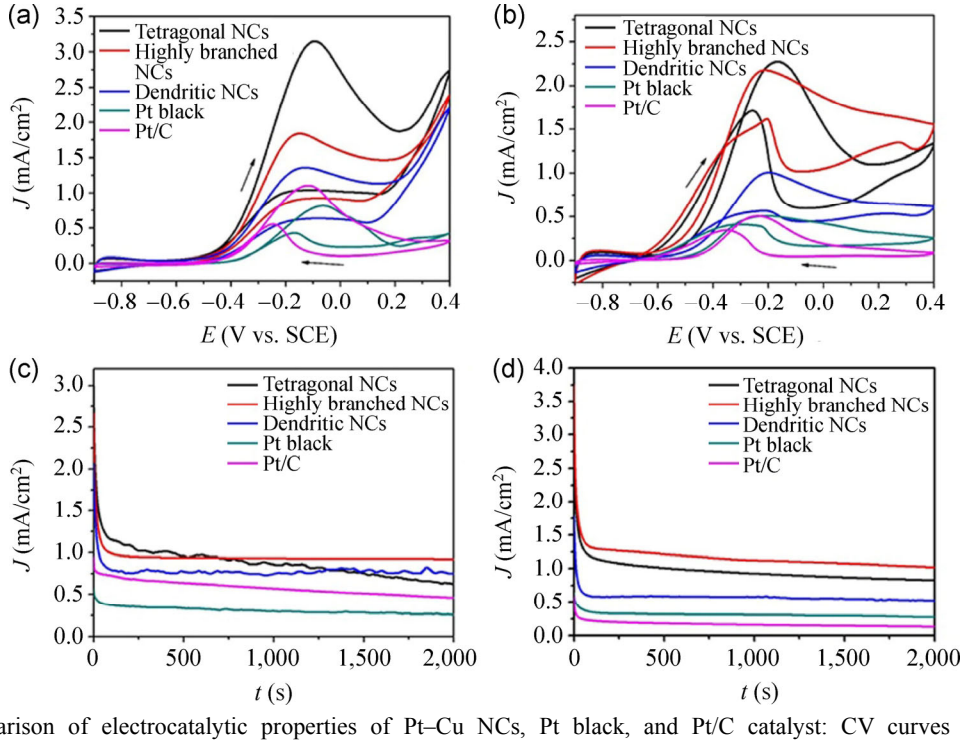

Figure 5 Comparison of electrocatalytic properties of Pt–Cu NCs, Pt black, and Pt/C catalyst: CV curves recorded at room temperature in (a) 0.5 M NaOH + 2 M methanol, and (b) 0.5 M NaOH + 0.1 M ethanol solution at a scan rate of 50 mV/s. Current–time (*i*–*t*) curves (at –0.2 V vs. SCE) in (c) methanol and (d) ethanol.

of methanol and ethanol on the tetragonal Pt–Cu superstructures, highly branched, small dendrites, commercial Pt black and Pt/C. The specific current density (J) was normalized to the electrochemically active surface area (ECSA), which was estimated from the hydrogen adsorption/desorption charges using cyclic voltammetric data in H_2SO_4 (0.5 M), assuming the charge density associated with a monolayer of hydrogen adsorbed on polycrystalline platinum is 210 μC/cm^2 (Fig. S21 in the ESM) [23, 27, 32]. The Pt–Cu superstructures exhibited enhanced specific activity compared with commercial Pt black and Pt/C catalysts, with the tetragonal Pt–Cu superstructures exhibiting the highest specific activity. The peak current density of methanol oxidation in the positive potential scan of tetragonal Pt–Cu superstructures was 3.2 mA/cm^2. This value is about 2 times that for the highly branched NCs, 1.8 times that for dendritic NCs, 4 times that for Pt black, and 3 times that for Pt/C. Similar results were also observed in case of ethanol electro-oxidation.

Taking into account the hierarchical structures of Pt–Cu with interconnected arms, the high electrocatalytic activity of the NCs compared with other catalysts can be attributed to their unique structure. To evaluate the stability of these Pt–Cu alloy NCs, i–t curves were recorded for 2,000 s (Figs. 5(c) and 5(d)). The Pt–Cu alloy NCs possess excellent stability during the electrochemical measurements, as compared with commercial Pt/C and Pt black catalysts. After the stability tests, the structure of the Pt–Cu alloy NCs was retained as shown in Fig. S22 (in the ESM).

In summary, we have developed a simple method for the synthesis of Pt–Cu hierarchical superstructures with well-defined 3D shapes. Tetragonal, highly branched, and dendritic superstructures consist of (111, 110), (111), and (100) planes, respectively. The shape of the complex architecture, particle size, and crystallinity can be controlled by tuning the amount of NaI. Among the different shapes, the tetragonal superstructures exhibited the best electrocatalytic activity, superior to those of commercial Pt/C, and Pt black. Further exploration of similar reaction systems may expand the present work to encompass the synthesis of other nanomaterials.

Acknowledgements

This work was supported by the National Natural Science Foundation of China (Nos. 91127040 and 21221062), and the State Key Project of Fundamental Research for Nanoscience and Nanotechnology (No. 2011CB932402).

Electronic Supplementary Material: Supplementary material (experimental details, additional SEM, TEM, HRTEM images, XRD patterns, EDX results, and electrocatalysis results) is available in the online version of this article at http://dx.doi.org/10.1007/s12274-014-0565-1.

References

[1] Chen, C.; Kang, Y. J; Huo, Z. Y.; Zhu, Z. W.; Huang, W. N.; Xin, H. L. L.; Snyder, J. D.; Li, Y. D. G.; Herron, J. A.; Mavrikakis, M. et al. Highly crystalline multimetallic nanoframes with three-dimensional electrocatalytic surfaces. *Science* **2014**, *343*, 1339–1343.

[2] Song, Y. J.; Yang, Y.; Medforth, C. J.; Pereira, E.; Singh, A. K.; Xu, H. F.; Jiang, Y. B.; Brinker, C. J.; Swol, F. V.; Shelnutt, J. A. Controlled synthesis of 2-D and 3-D dendritic platinum nanostructures. *J. Am. Chem. Soc.* **2004**, *126*, 635–645.

[3] Noorduin, W. L.; Grinthal, A.; Mahadevan, L.; Aizenberg, J. Rationally designed complex, hierarchical microarchitectures. *Science* **2013**, *340*, 832–836.

[4] Miszta, K.; Graaf, J. D.; Bertoni, G.; Dorfs, D.; Brescia, R.; Marras, S.; Ceseracciu, L.; Cingolani, R.; Roij, R. V.; Dijkstra, M. et al. Hierarchical self-assembly of suspended branched colloidal nanocrystals into superlattice structures. *Nat. Mater.* **2011**, *10*, 872–876.

[5] Gao, H. L.; Xu, L.; Long, F.; Pan, Z.; Du, Y. X.; Lu, Y.; Ge, J.; Yu, S. H. Macroscopic free-standing hierarchical 3D architectures assembled from silver nanowires by ice templating. *Angew. Chem. Int. Ed.* **2014**, *53*, 4561–4566.

[6] Jia, Y. Y.; Jiang, Y. Q.; Zhang, J. W.; Zhang, L.; Chen, Q. L.; Xie, Z. X.; Zheng, L. S. Unique excavated rhombic dodecahedral $PtCu_3$ alloy nanocrystals constructed with ultrathin nanosheets of high-energy {110} facets. *J. Am. Chem. Soc.* **2014**, *136*, 3748–3751.

[7] Nudelman, M.; Sommerdijk, N. A. J. M. Biomineralization as an inspiration for materials chemistry. *Angew. Chem. Int. Ed.* **2012**, *51*, 6582–6596.

[8] Bharathi, S.; Nataraj, D.; Seetha, M.; Mangalaraj, D.; Ponpandian, N.; Masuda, Y.; Senthil, K.; Yong, K. Controlled growth of single-crystalline, nanostructured dendrites and snowflakes of α-Fe_2O_3: Influence of the surfactant on the morphology and investigation of morphology dependent magnetic properties. *CrystEngComm*. **2010**, *12*, 373–382.

[9] Xiong, W. W.; Athresh, E. U.; Ng, Y. T.; Ding, J. F.; Wu, T.; Zhang, Q. H. Growing crystalline chalcogenidoarsenates in surfactants: From zero-dimensional cluster to three-dimensional framework. *J. Am. Chem. Soc.* **2013**, *135*, 1256–1259.

[10] Shi, L. H.; Wang, A. Q.; Zhang, T.; Zhang, B.; Su, D. S.; Li, H. Q.; Song, Y. J. One-step synthesis of Au–Pd alloy nanodendrites and their catalytic activity. *J. Phys. Chem. C* **2013**, *117*, 12526–12536.

[11] Wang, J. P.; Thomas, D. F.; Chen, A. C. Direct growth of novel alloyed PtAu nanodendrites. *Chem. Commun*. **2008**, 5010–5012.

[12] Lee, Y. W.; Kim, B. Y.; Lee, K. H.; Song, W. J.; Cao, G. Z.; Park, K. W. Synthesis of monodispersed Pt–Ni alloy nanodendrites and their electrochemical properties. *Int. J. Electrochem. Sci*. **2013**, *8*, 2305–2312.

[13] Lou, X. Y.; Yuan, C. L.; Archer, L. A. An unusual example of hyperbranched metal nanocrystals and their shape evolution. *Chem. Mater*. **2006**, *18*, 3921–3923.

[14] Mohanty, A.; Garg, N.; Jin, R. C. A universal approach to the synthesis of noble metal nanodendrites and their catalytic properties. *Angew. Chem. Int. Ed*. **2010**, *49*, 4962–4966.

[15] Lim, B. K.; Jiang, M. J.; Yu, T. Y.; Camargo, P. H. C.; Xia, Y. Nucleation and growth mechanisms for Pd–Pt bimetallic nanodendrites and their electrocatalytic properties. *Nano Res.* **2010**, *3*, 69–80.

[16] Teng, X. W.; Liang, X. Y.; Maksimuk, S.; Yang, H. Synthesis of porous platinum nanoparticles. *Small* **2006**, *2*, 249–253.

[17] Yin, J.; Wang, J. H.; Li, M. R.; Jin, C. Z.; Zhang, T. Iodine ions mediated formation of monomorphic single-crystalline platinum nanoflowers. *Chem. Mater*. **2012**, *24*, 2645–2654.

[18] Wang, F.; Li, C. H.; Sun, L. D.; Xu, C. H.; Wang, J. F.; Yu, J. C.; Yan, C. H. Porous single-crystalline palladium nanoparticles with high catalytic activities. *Angew. Chem. Int. Ed*. **2012**, *51*, 4872–4876.

[19] Niu, Z. Q.; Wang, D. S.; Yu, R.; Peng, Q.; Li, Y. D. Highly branched Pt–Ni nanocrystals enclosed by stepped surface for methanol oxidation. *Chem. Sci*. **2012**, *3*, 1925–1929.

[20] Zhu, L. P.; Xiao, H. M.; Zhang, W. D.; Yang, Y.; Fu, S. Y. Synthesis and characterization of novel three-dimensional metallic Co dendritic superstructures by a simple hydrothermal reduction route. *CrystalGrowthDes.* **2008**, *8*, 1113–1118.

[21] Wu, J. B.; Qi, L.; You, H. J.; Gross, A.; Li, J.; Yang, H. Icosahedral platinum alloy nanocrystals with enhanced electrocatalytic activities. *J. Am. Chem. Soc*. **2012**, *134*, 11880–11883.

[22] Wang, D. S.; Li, Y. D. Bimetallic nanocrystals: Liquid-phase synthesis and catalytic applications. *Adv. Mater.* **2011**, *23*, 1044–1060.

[23] Nosheen, F.; Zhang, Z. C.; Zhuang, J.; Wang, X. One-pot fabrication of single-crystalline octahedral Pt–Cu nanoframes and their enhanced electrocatalytic activity. *Nanoscale* **2013**, *5*, 3660–3663.

[24] Shao, M. H.; Shoemaker, K.; Peles, A.; Kaneko, K.; Protsailo, L. Pt monolayer on porous Pd–Cu alloys as oxygen reduction electrocatalysts. *J. Am. Chem. Soc*. **2010**, *132*, 9253–9255.

[25] Bing, Y.; Liu, H. H.; Zhang, L.; Ghosh, D.; Zhang, J. J. Nanostructured Pt-alloy electrocatalysts for PEM fuel cell oxygen reduction reaction. *Chem. Soc. Rev*. **2010**, *39*, 2184–2202.

[26] Hu, X. N.; Zhao, Y. Y.; Hu, Z. J.; Saran, A.; Hou, S.; Wen T.; Liu, W. Q; Ji, Y. L.; Jiang, X. Y.; Wu, X. C. Gold nanorods core/AgPt alloy nanodots shell: A novel potent antibacterial nanostructure. *Nano Res.* **2013**, *6*, 822–835.

[27] Zhang, Z. C.; Yang, Y.; Nosheen, F.; Wang, P. P.; Zhang, J. C.; Zhuang, J.; Wang, X. Fine tuning of the structure of Pt–Cu alloy nanocrystals by glycine-mediated sequential reduction kinetics. *Small* **2013**, *9*, 3063–3069.

[28] Zheng, F. L.; Wong, W. T.; Yung, K. F. Facile design of Au@Pt core–shell nanostructures: Formation of Pt submonolayers with tunable coverage and their applications in electrocatalysis. *Nano Res.* **2014**, *7*, 410–417.

[29] Zhang, Q.; Guo, X.; Liang, Z. X.; Zeng, J. H.; Yang, Y.; Liao, S. J. Hybrid PdAg alloy–Au nanorods: Controlled growth, optical properties and electrochemical catalysis. *Nano Res*. **2013**, 6, 571–580.

[30] Lim, B. K.; Jiang, M. J.; Camargo, P. H. C.; Cho, E. C.; Tao, J.; Lu, X. M.; Zhu, Y. M.; Xia, Y. Pd–Pt bimetallic nanodendrites with high activity for oxygen reduction. *Science* **2009**, *324*, 1302–1305.

[31] Fan, N.; Yang, Y.; Wang, W. F.; Zhang, L. J.; Chen, W.; Zou, C.; Huang, S. M. Selective etching induces selective growth and controlled formation of various platinum nanostructures by modifying seed surface free energy. *ACS Nano* **2012**, *6*, 4072–4082.

[32] Zhang, Z. C.; Nosheen, F.; Zhang, J. C.; Yang, Y.; Wang, P. P.; Zhuang, J.; Wang, X. Growth of concave polyhedral Pd nanocrystals with 32 facets through *in situ* facet-selective etching. *ChemSusChem* **2013**, *6*, 1893–1897.